

X-ray emissions from two-temperature accretion flows within a dipole magnetic funnel

Curtis J. Saxton¹, Kinwah Wu^{1,2}, João. B. G. Canalle³, Mark Cropper¹
& Gavin Ramsay^{1,4}

¹ *Mullard Space Science Laboratory, University College London, Holmbury St Mary, Dorking, Surrey RH5 6NT, England*

² *TIARA, Department of Physics, National Tsing Hua University, Hsinchu 300, Taiwan*

³ *State University of Rio de Janeiro, Rua São Francisco Xavier, 524/3023-D, CEP 20559-900, Rio de Janeiro, RJ, Brazil*

⁴ *Armagh Observatory, College Hill, Armagh BT61 9DG, N. Ireland*

Accepted —. Received —; in original form —

ABSTRACT

We investigate the hydrodynamics of accretion channelled by a dipolar magnetic field (funnel flows). We consider situations in which the electrons and ions in the flow cannot maintain thermal equilibrium (two-temperature effects) due to strong radiative loss, and determine the effects on the keV X-ray properties of the systems. We apply this model to investigate the accretion shocks of white dwarfs in magnetic cataclysmic variables. We have found that the incorporation of two-temperature effects could harden the keV X-rays. Also, the dipolar model yields harder X-ray spectra than the standard planar model if white dwarf is sufficiently massive ($\gtrsim 1M_{\odot}$). When fitting observed keV X-ray spectra of magnetic cataclysmic variables, the inclusion of two-temperature hydrodynamics and a dipolar accretion geometry lowers estimates for white-dwarf masses when compared with masses inferred from models excluding these effects. We find mass reductions $\lesssim 9\%$ in the most massive cases.

Key words: accretion, accretion discs — hydrodynamics — shock waves — stars: binaries: close — stars: white dwarfs — X-rays: binaries

1 INTRODUCTION

Field-channelled accretion occurs in a variety of stellar systems, from young stellar objects (e.g. Königl 1991; Hartman et al. 1994; Gullbring et al. 2000; Lamzin et al. 2001; Romanova et al. 2003; Stelzer & Schmitt 2004; Gregory et al. 2006) to compact stars (e.g. Elsner & Lamb 1977; Ghosh & Lamb 1978; Arons 1993; Lovelace et al. 1995; Li et al. 1996; Li & Wilson 1999; Kryukov et al. 2000; Koldoba et al. 2002; Toropina et al. 2003; Canalle et al. 2005), where the magnetic stress of the accretor exceeds the ram pressure of the accretion flow. For accretion onto white dwarfs in magnetic cataclysmic variables (mCVs) (Warner 1995; Cropper 1990), the magnetic field not only directs the flow but could also dictate the radiative-loss processes (see e.g. Wu et al. 2003). This, in turn, alters the flow hydrodynamics, leading to observable consequences, for example, in the optical/IR polarisation and keV X-ray spectra of the system.

The keV X-ray emitting regions of mCVs are usually located at the magnetic field footpoints on the white-dwarf surface. Here an optically thin plasma slab heated by a strong shock, at which the supersonic flows in the upstream

region decelerate abruptly to attain subsonic speeds. Typically, the shock temperature is $T \approx 3GM_w m_H / 8kR_w \sim 10 - 50$ keV (where G is the gravitational constant, k is the Boltzmann constant, m_H is the hydrogen atomic mass, M_w is the white-dwarf mass, R_w is the white-dwarf radius). The shock-heated flow is cooled by emission of free-free and line X-rays, and optical/IR cyclotron radiation.

The post-shock regions of white dwarfs in mCVs are stratified in temperature and density, and the flow structures are in general well described by Aizu-type models (Aizu 1973; Chevalier & Imamura 1982; Wu 1994; Wu et al. 1994; Cropper et al. 1999; Wu 2000). These models assume that the electron and ions are in thermal equilibrium, via collisions, and share the same local temperature. (Hereafter, these models are denoted as standard one-temperature (1T) models.) The standard 1T models have successfully explained the line features in the keV X-ray spectra of mCVs. However using the standard 1T models to generate spectral fits for mCVs tends to require white-dwarf masses systematically higher than the masses measured by other techniques (see Ramsay et al. 1998; Ramsay 2000). This has led to questions on the validity the 1T approximation.

It has long been recognised (Fabian et al. 1976;

King & Lasota 1979; Lamb & Masters 1979) that the electrons and ions in the post-shock flows of mCVs might be unable to maintain thermal equilibrium solely via electron-ion collisions (see also Imamura 1981; Imamura et al. 1987, 1996; Woelk & Beuermann 1996; Saxton & Wu 1999, 2001; Fischer & Beuermann 2001). The departure of the electron temperature from the ion temperature can be severe if the radiative-loss timescale of the flow is much shorter than the dynamical timescale. In such situations, two-temperature (2T) effects on the X-ray spectra are no longer negligible. Two-temperature effects on X-ray spectra of mCVs were previously investigated assuming planar stratified flow (Saxton et al. 2005). However, the accretion flows in mCVs are not planar. There is evidence that the accretion flows form curved funnel/curtain-like columns along the magnetic field lines (Ferrario 1996; Heerlein et al. 1999). The hydrodynamics in funnel flow and in planar are qualitatively different, especially for tall post-shock columns where a variation of the gravitational potential is significant (Canalle et al. 2005).

Here we investigate 2T accretion in mCVs where the flows are guided by the white-dwarf magnetic field geometry. This work is a generalisation of both the 2T planar flow calculations of Saxton et al. (2005) and the 1T dipole-field channelled flow calculations of Canalle et al. (2005). We organise the paper as follows. In §2 we present the model assumptions and the hydrodynamic formulation; in §3 we show the hydrodynamical structures and X-ray spectra obtained from the calculations and discuss the properties of the flows (and their dependence on system parameters). In §4 we summarise the major findings.

2 HYDRODYNAMIC FORMULATION

For a gas with adiabatic index γ , density ρ , velocity \mathbf{v} and pressure P , subject to a gravitational field \mathbf{g} , the general hydrodynamic equations for conservation of mass, momentum and energy can be expressed as

$$\frac{\partial \rho}{\partial t} + \nabla \cdot \rho \mathbf{v} = 0, \quad (1)$$

$$\frac{\partial}{\partial t} \rho \mathbf{v} + \nabla \cdot \rho \mathbf{v} \mathbf{v} + \nabla P = \rho \mathbf{g}, \quad (2)$$

and

$$\left(\frac{\partial}{\partial t} + \mathbf{v} \cdot \nabla \right) P - \frac{\gamma P}{\rho} \left(\frac{\partial}{\partial t} + \mathbf{v} \cdot \nabla \right) \rho = -(\gamma - 1)\Lambda, \quad (3)$$

where Λ is the volumetric energy loss rate due to radiative cooling. Emission by electrons far exceeds emission by the ions. Unlike Canalle et al. (2005), who assumed temperature equilibrium between electrons and ions, we will consider cases where electron radiative cooling is significant compared to collisional heating by the ions. This entails a separate energy equation for the electron sub-fluid,

$$\left(\frac{\partial}{\partial t} + \mathbf{v} \cdot \nabla \right) P_e - \frac{\gamma P_e}{\rho} \left(\frac{\partial}{\partial t} + \mathbf{v} \cdot \nabla \right) \rho = (\gamma - 1)(\Gamma - \Lambda), \quad (4)$$

where P_e is the electron partial pressure. The electron cooling function, $\Lambda = \Lambda(\rho, P_e)$, and the collisional heating function, $\Gamma = \Gamma(\rho, P, P_e)$, depend on local hydrodynamic variables (Spitzer 1962; Rybicki & Lightman 1979; Imamura et al. 1996).

We consider accretion flows that are channelled by a dipolar magnetic field centred on the accreting stellar object. The coordinate w measures paths along a magnetic field line towards the accretor. A transverse coordinate $u = \sin^2 \theta_*$ is related to the colatitude of the accretion hot-spot (θ_*). The azimuthal angle φ is the same as in cylindrical coordinates. We seek stationary solutions for the flow structure, so we omit temporal derivatives from (1)–(4). We recast the equations in curvilinear coordinates, $(\hat{\mathbf{u}}, \hat{\mathbf{w}}, \hat{\boldsymbol{\varphi}})$. For flows along the field line, there is no velocity component in the $\hat{\mathbf{u}}$ or $\hat{\boldsymbol{\varphi}}$ directions. Then the hydrodynamic equations for mass flux, momentum flux, total energy and electron energy simplify to

$$\frac{\partial}{\partial w} h_1 h_3 \rho v = 0 \Rightarrow h_1 h_3 \rho v = C, \quad (5)$$

$$\frac{v}{h_2} \frac{\partial v}{\partial w} + \frac{1}{h_2 \rho} \frac{\partial P}{\partial w} = g_w, \quad (6)$$

$$\frac{v}{h_2} \frac{\partial P}{\partial w} - \frac{\gamma}{h_2} \frac{P v}{\rho} \frac{\partial \rho}{\partial w} = -(\gamma - 1)\Lambda, \quad (7)$$

$$\frac{v}{h_2} \frac{\partial P_e}{\partial w} - \frac{\gamma}{h_2} \frac{P_e v}{\rho} \frac{\partial \rho}{\partial w} = -(\gamma - 1)(\Lambda - \Gamma), \quad (8)$$

where C is a constant proportional to the mass flux onto the stellar surface, $C = \dot{m} h_{1*} h_{3*}$. The functions $h_1(u, w)$ and $h_3(u, w)$ are metric terms of the curvilinear coordinate system (see Appendix A). The term $g_w = \mathbf{g} \cdot \hat{\mathbf{w}}$ is gravitational acceleration along the magnetic field line (i.e. in the w direction).

As expressed in Saxton et al. (2005), the rate of energy exchange from ions to electrons has the form

$$\Gamma = X \rho^{5/2} P_e^{-3/2} (P - \chi P_e), \quad (9)$$

where X and χ are numerical constants that depend on the plasma composition. The volumetric cooling rate of gas due to thermal bremsstrahlung radiation is approximated as

$$\Lambda_{\text{br}} = A \rho^2 \sqrt{\frac{P_e}{\rho}}, \quad (10)$$

with A being another constant depending on composition. Saxton et al. (2005) gave derivations of A , X and χ and their values for a plasma of solar metallicity. We assume a total cooling function that includes bremsstrahlung and cyclotron contributions,

$$\Lambda = \Lambda_{\text{br}} + \Lambda_{\text{cy}} = \Lambda_{\text{br}} [1 + \epsilon_s f_{\text{cy}}(\rho, P_e)], \quad (11)$$

with a cyclotron/bremsstrahlung emissivity ratio given by the function f_{cy} defined by Wu (1994); Wu et al. (1994); Saxton et al. (1997), refined by Saxton & Wu (1999); Cropper et al. (1999); Saxton et al. (2005) and extended to the dipolar accretion model in Canalle et al. (2005).

We rewrite the flow density, total pressure and electron partial pressure in terms of the h functions, the flow constant C and variables that have the dimensions of velocity,

$$\rho = \frac{C}{h_1 h_3 v}, \quad (12)$$

$$P = \frac{C}{h_1 h_3} (\xi - v), \quad (13)$$

$$P_e = \frac{C}{h_1 h_3} (\xi - v) \left(\frac{\sigma}{\sigma + 1} \right), \quad (14)$$

where ξ measures the ratio of momentum to mass fluxes (introduced in Cropper et al. 1999) and $\sigma \equiv P_e/P_i$, the electron to ion partial pressure ratio. For the sake of further brevity, we define

$$p \equiv \frac{h_1 h_3}{C} P_e = \frac{\sigma}{\sigma + 1} (\xi - v). \quad (15)$$

We separate the finite and v^{-1} terms in the electron-ion energy exchange function and the bremsstrahlung radiative cooling functions,

$$\Gamma = X \left(\frac{C}{h_1 h_3} \right)^2 \frac{\sigma + 1 - \chi \sigma}{\sigma p^{1/2} v^{5/2}} \equiv \frac{C}{h_1 h_2 h_3} \hat{\Gamma} v^{-5/2}, \quad (16)$$

$$\Lambda_{\text{br}} = A \left(\frac{C}{h_1 h_3} \right)^2 p^{1/2} v^{-3/2} \equiv \frac{C}{h_1 h_2 h_3} \tilde{\Lambda} v^{-3/2}. \quad (17)$$

The functions $\hat{\Gamma} \equiv h_1 h_2 h_3 \Gamma v^{5/2}/C$ and $\tilde{\Lambda} \equiv h_1 h_2 h_3 \Lambda v^{3/2}/C$ lack explicit v dependencies and are finite everywhere.

As in Canalle et al. (2005), the equations for momentum and total energy provide

$$\frac{d\xi}{dw} = \frac{g_w h_2}{v} + \mathcal{H}(\xi - v), \quad (18)$$

$$\frac{dv}{dw} = \frac{-[(\gamma - 1)\tilde{\Lambda} v^{-3/2} + \gamma \mathcal{H}(\xi - v)v + h_2 g_w]}{\gamma(\xi - v) - v}. \quad (19)$$

Definition (14), equations (6) and (19) yield

$$\frac{dP_e}{dw} = \frac{P_e}{\xi - v} \left(\frac{d\xi}{dw} - \frac{dv}{dw} \right) - \mathcal{H}P_e + \frac{(P - P_e)^2}{P} \frac{d\sigma}{dw}, \quad (20)$$

$$\frac{d\sigma}{dw} = -\frac{(\gamma - 1)(\sigma + 1)}{(\xi - v)v^{7/2}} [v\tilde{\Lambda} - (\sigma + 1)\hat{\Gamma}]. \quad (21)$$

Strong shock conditions apply at the outer boundary, while the condition $v = 0$ applies at the stellar surface ($r = 1$). Our particular method of numerical solution is described in Appendix B. We adopt the white dwarf mass-radius relation of Nauenberg (1972).

3 RESULTS

3.1 Structure of the post-shock flow

Table 1 summarises the basic properties of several models of mCVs, with nearly direct (approximately radial) accretion onto a magnetic pole (colatitude $\theta_* = 0.001^\circ$) and hot-spot area 10^{15} cm^2 . We consider white dwarfs in the mass range $0.7 - 1.2M_\odot$, with surface magnetic field strengths $B_* \leq 50 \text{ MG}$. The ratio of electron to ion temperatures at the shock, $(T_e/T_i)_s$, is treated as a free parameter (e.g. as in Imamura et al. 1996; Saxton & Wu 1999; Saxton et al. 2005). This ratio has little effect on the shock height, R_s . This implies that the shock position is insensitive to the details of heating at the shock precursor, but depends mainly on the white-dwarf's properties, the inflow rate and field geometry.

Figure 1 shows how the shock radius varies with the accretion colatitude θ_* , the magnetic field strength and accretion rate. These illustrative models assume that $T_e = T_i$ at the shock, and accretion hot-spot area of 10^{15} cm^2 . In all calculations (as in Canalle et al. 2005) the shock is closer to the stellar surface when \dot{m} is greater. The greatest variation of R_s with θ_* occurs in systems where the shock radius is

Table 1. Parameters and properties of a set of representative accretion shocks, varying the electron to ion temperature ratio at the shock ($T_{e,s}/T_{i,s}$). The white-dwarf surface magnetic field is given by $B_7 = B_*/10 \text{ MG}$, and the specific accretion rate \dot{m} is in units of $\text{g cm}^{-2} \text{ s}^{-1}$. If the magnetic field at the hot-spot is B_* then its magnitude at the pole is $B_p = 2B_*/\sqrt{4 - 3u}$.

$T_{e,s}/T_{i,s} :$				1.0		0.5	
M_w	B_7	\dot{m}	θ_*	a_{15}	r_s	r_s	r_s
0.7	0.0	1.0	0.0	1.0	1.081	1.080	
0.7	1.0	1.0	0.0	1.0	1.047	1.047	
0.7	3.0	1.0	0.0	1.0	1.010	1.011	
0.7	5.0	1.0	0.0	1.0	1.005	1.005	
1.0	0.0	1.0	0.0	1.0	1.610	1.617	
1.0	1.0	1.0	0.0	1.0	1.096	1.103	
1.0	3.0	1.0	0.0	1.0	1.015	1.017	
1.0	5.0	1.0	0.0	1.0	1.007	1.008	
1.2	1.0	1.0	0.0	1.0	1.175	1.206	
1.2	3.0	1.0	0.0	1.0	1.024	1.028	
1.2	5.0	1.0	0.0	1.0	1.011	1.014	

large compared to R_w . We find that the 1T model (dotted curves) predicts lower shock positions than the 2T model does. The difference is proportionally greater in large- B_* cases, where the shock is typically nearer the stellar surface. As the 2T model predicts increased R_s values, the shock temperatures are lower, $T_s \propto R_s^{-1}$. This effect is greatest for large M_w .

Figure 2 portrays the radial distribution of electron density (n_e) and temperature (kT_e) in accretion models with $\theta_* = 0^\circ$, $M_w = 1.0M_\odot$ and $\dot{m} = 2 \text{ g cm}^{-2} \text{ s}^{-1}$. The 1T and 2T models predict similar density and thermal structures in the lower field cases ($B_* = 0 \text{ MG}$). However for stronger magnetic fields ($B_* = 50 \text{ MG}$) the models predict considerably different shock heights and qualitatively different density and temperature distributions. In 2T structures, the hottest electrons are confined to a narrower region near the shock than in 1T shocks with equivalent system parameters. Plotting the T_e versus n_e distributions, as in the lower panels of Figure 2, shows that in 2T models with strong magnetic fields the density of the hottest gas is lower than in 1T models. This will have consequences for the post-shock X-ray emissions.

3.2 X-ray emissions

For each of the solutions for the post-shock accretion flow, we calculate an X-ray spectrum following the methods of Cropper et al. (1999) and Saxton et al. (2005). The post-shock volume is divided into $\gtrsim 10^4$ strata according to the spatial steps of the numerically integrated flow profile. The volume of each stratum is inferred from the step size du , the hot-spot area and the cross-sectional area scaling factor $h_1 h_3 / h_{1*} h_{3*}$. The local electron density and temperature (n_e, T_e) are obtained from the dimensionless flow model and the scaling units, (R_w, V_w, C) . We assume that the X-ray line and continuum emission are optically thin, and in-

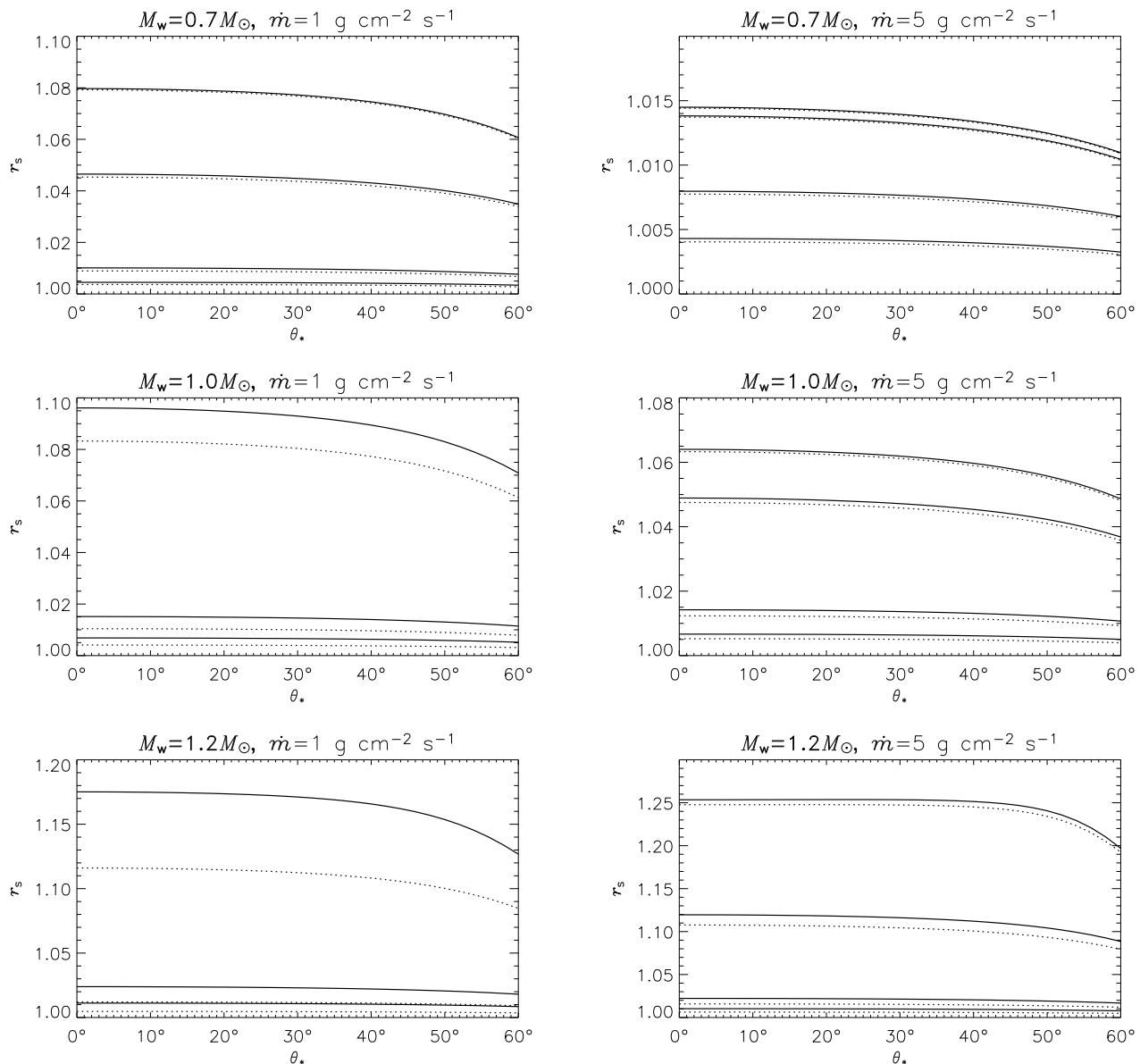


Figure 1. Effect of the accretion colatitude (θ_*) upon the shock radius, $r_s \equiv R_s/R_w$ in units of the stellar radius, for cases with different specific accretion rates (\dot{m}), white-dwarf mass (M_w) and magnetic field (B_*). The accretion hot-spot area is 10^{15} cm^2 . Solid lines mark the results of the 2T model; dotted lines denote the corresponding results of the 1T model. Within each panel, paired curves from bottom to top represent cases with field strengths $B_* = 50, 30, 10 \text{ MG}$; a fourth pair shows cases with negligible cyclotron cooling (yet channelled by a dipole funnel). These low-field cases are insoluble when $\dot{m} = 1 \text{ g cm}^{-2} \text{ s}^{-1}$, and $M_w = 1.0, 1.2 M_\odot$.

voke the XSPEC implementation of the MEKAL thermal plasma model (Mewe et al. 1985; Kaastra & Mewe 1993) to calculate emissivities for local (n_e, T_e) values. Volumetric integration over all the post-shock strata yields a synthetic X-ray spectrum. We exclude the densest strata, with $n_e \geq 10^{18} \text{ cm}^{-3}$, which the spectral model cannot handle (and which in any case represent optically thick layers merging into the atmosphere of the white dwarf). We omit the effect of shadowing by a white dwarf which obscures its own accretion inflow.

Saxton et al. (2005) studied 2T effects in a planar accretion model, without the effects of gravity and varying width of the magnetic accretion funnel. They found that 2T effects

change the keV X-ray spectra most significantly for cases with larger M_w . For given system parameters, the 2T model gave a harder continuum but relatively weaker line emission. The ratio of electron to ion temperatures at the shock was found to have little effect on the spectra. This was explained in terms of the concentration of X-ray emission near the stellar surface (well downstream from the shock) by which point collisional energy exchanges have nearly equilibrated the electrons and ions.

Our present calculations, with a dipolar accretion funnel and 2T effects, typically produce spectra such as those in Figure 3. The slope of the continuum is steep, but there are variations in the curvature of the continuum and the details

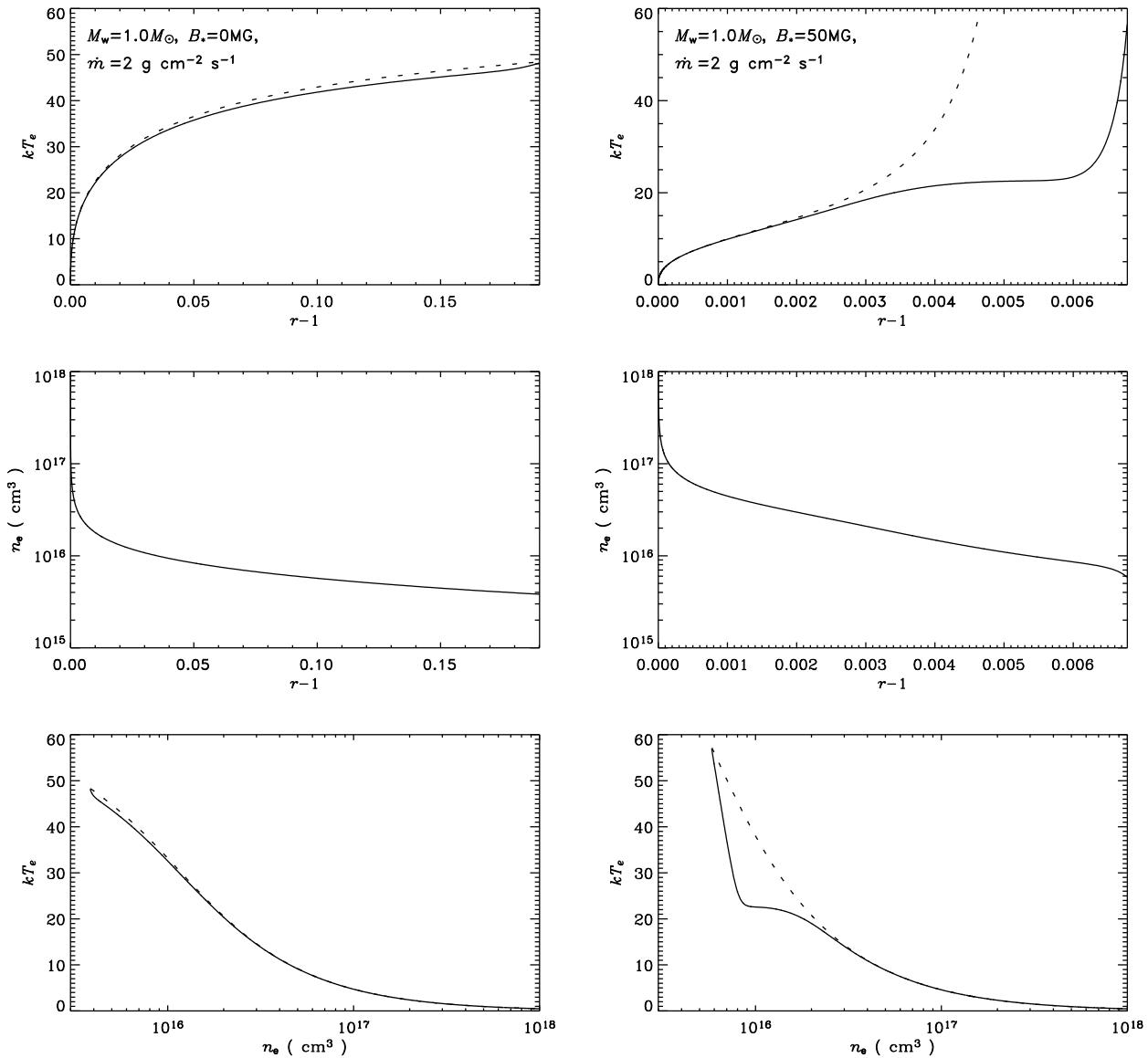


Figure 2. Profiles of electron temperature (upper row) and electron number density (middle row) for accretion onto $1.0 M_{\odot}$ white dwarfs, as a function of height above the surface. The left and right columns respectively show cases with negligible cyclotron cooling, and with dominant cyclotron cooling. The accretion spot is at the pole ($\theta_* = 0^\circ$). Solid lines mark the results of the 2T model; dotted lines denote the results of the 1T model. Electron and ion temperatures match at the shock and stellar surface, but the electrons are cooler elsewhere. The bottom row shows the temperature/density phase structure: in high-field cases the 2T model has lower densities in the hotter strata.

of line strengths. The effects of the various system parameters are best illustrated by plots of the ratios of spectra calculated with different conditions or assumptions.

3.2.1 Dipolar vs planar accretion

Figure 4 shows the ratios of X-ray spectra calculated in 2T models with identical system parameters but dipolar versus planar accretion geometry. In all the cases we calculated, the dipolar model provides a harder continuum, and reduced line emission, particularly for photon energies $\lesssim 1$ keV. These effects are small for a white dwarf of $0.7M_{\odot}$, but are more

considerable for $1.0M_{\odot}$ and more massive cases. The dipolar (2Td) and planar (2Tp) models are more in agreement regarding continuum at photon energies $\lesssim 1$ keV if the accretion hot-spot is at high θ_* (further from the magnetic pole).

3.2.2 Two-temperature vs one-temperature dipolar inflows

Figure 5 shows the quotients of X-ray spectra over the 0.2–10 keV band, from 1T and 2T dipolar calculations for a white-dwarf mass of $0.7M_{\odot}$. The X-ray continuum is generally brighter in a 2T model. In cases where bremsstrahlung

is the dominant cooling process ($B_* = 0$ MG) the X-ray continuum has equivalent spectral slopes in 1Td and 2Td models, up to photon energies ~ 5 keV. Above this energy, the 1Td model predicts a marginally harder continuum. The 1Td models predict $\sim 0.5\%$ stronger emission lines around 1 keV, but lines around ~ 7 keV are weakened by a similar degree.

For non-zero but small magnetic fields ($B_* = 10$ MG) the shape of the continuum is similar to the zero-field cases, but the 1Td and 2Td calculations yield greater discrepancies about the line strengths, up to $\sim 1\%$. The specific accretion rate, \dot{m} , has a slightly greater effect on the disagreements between the predicted lines.

For a stronger magnetic field ($B_* = 30$ MG) the 1Td model yields a softer continuum than equivalent 2Td calculations. The 1Td model generally predicts stronger emission lines, by up to $\sim 2\%$ for the cases with lowest \dot{m} . Two-temperature effects are less apparent in the keV X-ray continuum and lines when the accretion rate is larger. The spectral effects generally strengthen as the magnetic field increases; the greatest extreme in our plots is the case with $B_* = 50$ MG and $\dot{m} = 1 \text{ g cm}^{-2} \text{ s}^{-1}$.

The discrepancy between spectra predicted in the 1Td and 2Td models is more acute for systems with larger white-dwarf mass. For cases with $M_w = 1.0M_\odot$ (see Figure 6) the oversoftness of the 1Td predicted continuum is more pronounced in the $B_* = 30$ MG case than in the comparable $B_* = 50$ MG cases with $M_w = 0.7M_\odot$. The 1Td/2Td pattern of over- and under-prediction of line emission between ~ 7 keV and ~ 9 keV varies considerably with B_* and \dot{m} (see the upper right panels of Figure 6).

For systems with a white dwarf with $M_w = 1.2M_\odot$, the discrepancies are even greater than for $M_w = 1.0M_\odot$ cases: the continuum around ~ 10 keV can be around 10% under-predicted in the 1Td model, relative to the 2Td calculation (Figure 7). A downward spike in the H-like Fe K α emission that appears for $1.0M_\odot$ cases (in Figure 6, representing under-prediction of this line by the 1Td model) is absent when $M_w = 1.2M_\odot$, with all other parameters equal.

3.2.3 Latitude dependence

The X-ray spectrum also varies with the location of the accretion spot on the white-dwarf surface. Latitudinal effects are slight when the shock height is small compared to the stellar radius (e.g. $M_w = 0.7M_\odot$, $\dot{m} = 5 \text{ g cm}^{-2} \text{ s}^{-1}$); then we obtain $\lesssim 2\%$ enhancements in the ~ 1 keV lines. For the same white-dwarf mass but lower accretion rate (e.g. $M_w = 0.7M_\odot$, $\dot{m} = 1 \text{ g cm}^{-2} \text{ s}^{-1}$), a low-latitude accretion stream provides a softer X-ray continuum than polar accretion. Figure 8 shows the ratios of spectra: for inclined accretion cases ($\theta_* = 10^\circ, 30^\circ$ and 60°) compared to vertical accretion onto the pole ($\theta_* = 0^\circ$). For low-latitude accretion, lines are enhanced up to $\lesssim 20\%$ at photon energies $\lesssim 1$ keV. In the cases with $M_w = 0.7M_\odot$, the size of θ_* -dependency appears comparable for systems with low and high magnetic field strengths.

However in systems with a more massive white dwarf, $M_w = 1.2M_\odot$, the emission depends more sensitively on θ_* , for any field strength B_* . In the cases with the shock at a relatively low radius (e.g. $M_w = 1.2M_\odot$, $\dot{m} = 5 \text{ g cm}^{-2} \text{ s}^{-1}$) the spectra are almost indistinguishable for $\theta_* = 0^\circ, 10^\circ$;

the $\theta_* = 30^\circ$ cases differ from $\theta_* = 0^\circ$ by $\lesssim 1\%$ in the ~ 1 keV lines. At $\theta_* = 60^\circ$ the enhancement of line emission is $\lesssim 7\%$ when $B_* = 10$ MG, but half as great when $B_* = 50$ MG. A similar variation with B_* occurs among cases with $M_w = 1.2M_\odot$ and $\dot{m} = 1 \text{ g cm}^{-2} \text{ s}^{-1}$ — the greatest θ_* -dependency appears in the systems with the greatest relative shock height, r_s .

4 DISCUSSION

4.1 Summary for magnetic cataclysmic variables

The incorporation of 2T effects in the post-shock accretion flows of mCVs generally hardens the emitted keV X-ray continuum. A dipolar accretion funnel further hardens the spectrum of a 2T flow, relative to models with simpler planar geometry. A 2T dipolar model predicts a harder spectrum than a 2T planar model, if the white dwarf is as massive as $1M_\odot$ or more. The differences between planar and dipolar 2T accretion models are greatest in systems where the shock height is large compared to the stellar radius: i.e. greater M_w or lower B_* . The spectral predictions of 1T and 2T dipolar models differ more significantly when the white dwarf is massive, has a strong magnetic field or low specific accretion rate. Line emission is typically weaker around ~ 1 keV and $\sim 7 - 10$ keV in a 2T flow than in a 1T flow, except for the Fe K α lines, which could become stronger.

This is qualitatively consistent with the 2T effects found for basic planar accretion models without the inclusion of gravity in the hydrodynamic equations (Saxton et al. 2005); Two-temperature effects upon X-ray spectra persist despite the introduction of a dipolar magnetic field geometry, which in the 1T model of Canalle et al. (2005) soften the X-ray spectra relative to the results of Cropper et al. (1999). This softening due to funnel geometry is, however, smaller than the hardening apparent when 2T physics is incorporated. The 2Td model predicts the most hard photons for a given mass M_w , and therefore its spectral fit to an observed spectrum will require a lower mass than the standard planar and 1T models do.

4.2 Inferred masses

To quantify how the mass estimates are affected, we calculated spectra for models with different M_w , with the other parameters fixed ($\theta_* = 0^\circ$, $\dot{m} = 2 \text{ g cm}^{-2} \text{ s}^{-1}$), for medium ($B_* = 20$ MG) and strong-field ($B_* = 50$ MG) cases. For a given white dwarf mass, we manually match the shape of the X-ray continuum by adjusting the masses in 1Tp, 1Td, 2Tp and 2Td models (Wu 1994; Canalle et al. 2005; Saxton et al. 2005, this paper respectively). Each fit is defined by matching the ratio of spectra at 0.1 keV and 10 keV, with the flattest possible ratio at intermediate energies. Figure 9 illustrates how the 2T and dipolar funnel effects change spectral inferences of the white dwarf mass (M_w) from X-ray observations. For low-mass white dwarfs ($M_w \approx 0.5M_\odot$) the 1T and 2T spectral predictions are similar. However for cases with higher mass, say $M_w \gtrsim 1.0M_\odot$, the spectra differ considerably (middle panels).

For large M_w , the 2Tp models require lower masses than 1Tp models. For $B_* = 50$ MG the 1Td model requires

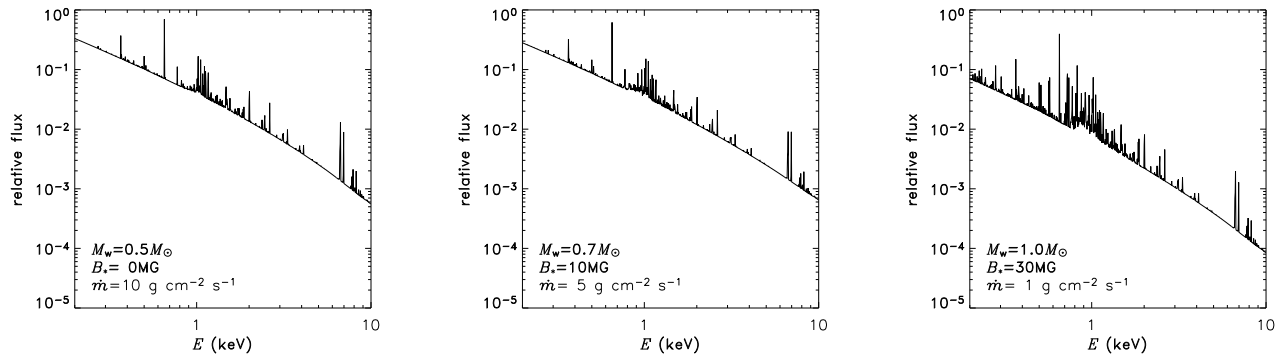


Figure 3. X-ray spectra for photon energies 0.2 – 10 keV, calculated for dipole-field channelled 2T accretion onto white dwarfs with parameters as indicated in the panels.

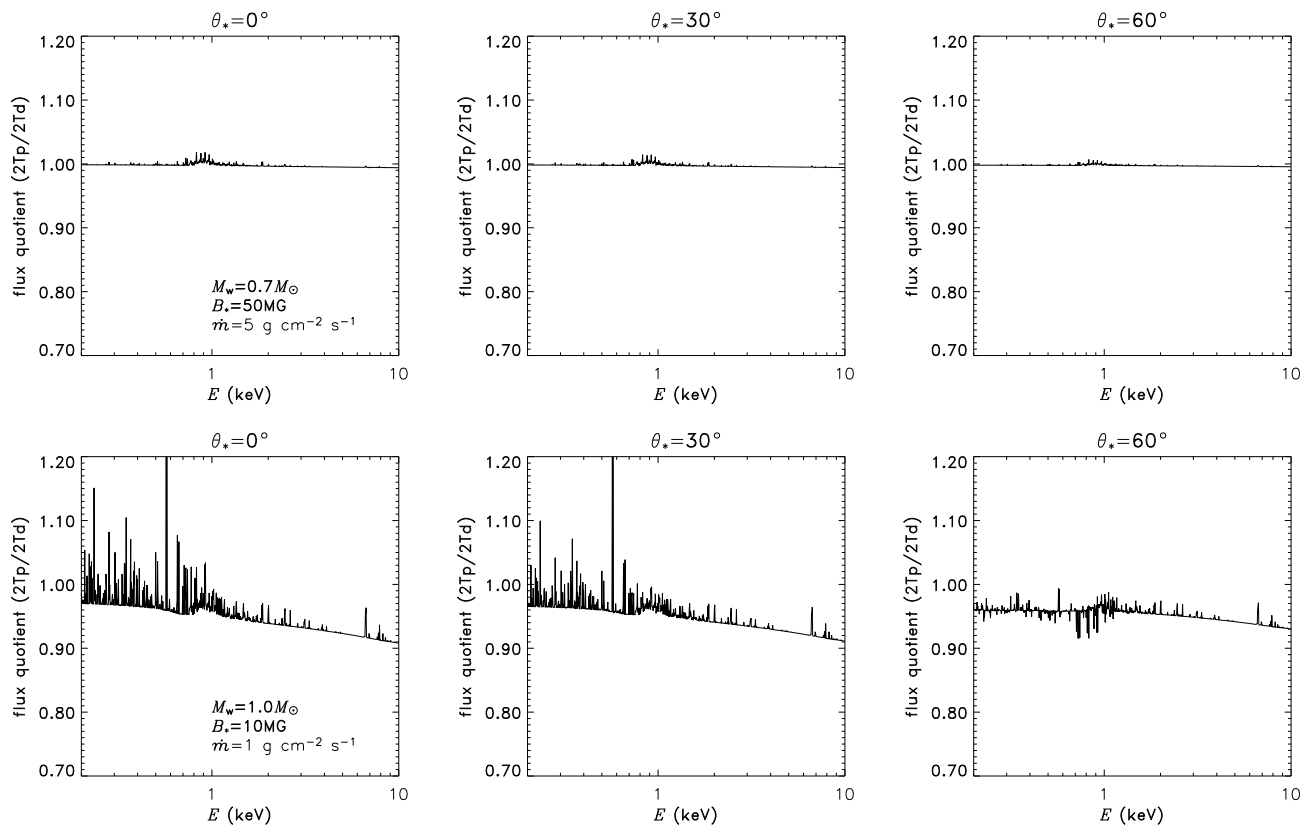


Figure 4. Quotients of spectra in 2T planar accretion model to spectra in the corresponding dipolar accretion model (2Tp/2Td). The columns show different cases of the accretion colatitude, θ_* = 0°, 30°, 60°. The top row represents a system in which the shock height is small compared to the stellar radius. The bottom row shows a system with a relatively high shock. In the latter, spectra differ significantly between the dipolar and planar models.

greater masses than 2Tp models; but for $B_* = 20$ MG the 1Tp model is more massive. The 2T dipolar models consistently need the lowest M_w (see corresponding fitted masses in Figure 10). The introduction of dipolar geometry to 2-temperature flows (from 2Tp to 2Td models) has hardened the spectra. For example, a $1.00M_\odot$ 2Tp model matches a 2Td model with $M_w \approx 0.98M_\odot$ (i.e. a 2% discrepancy, see Table 2). The X-ray continuum of a $1.00M_\odot$ 1Td model is

best matches a 2Td model with $M_w \approx 0.95M_\odot$ (a 5% discrepancy, see Figure 9, lower middle panel).

We note that the flow geometry and 2T conditions can affect the line spectra as well as the continuum. Here, we demonstrate that mass estimates obtained from the continuum fitting depends on the assumed geometry of the flow. If the spectral line information were also considered, we would need to consider variations of the values of B_* , \dot{m} , θ_* and

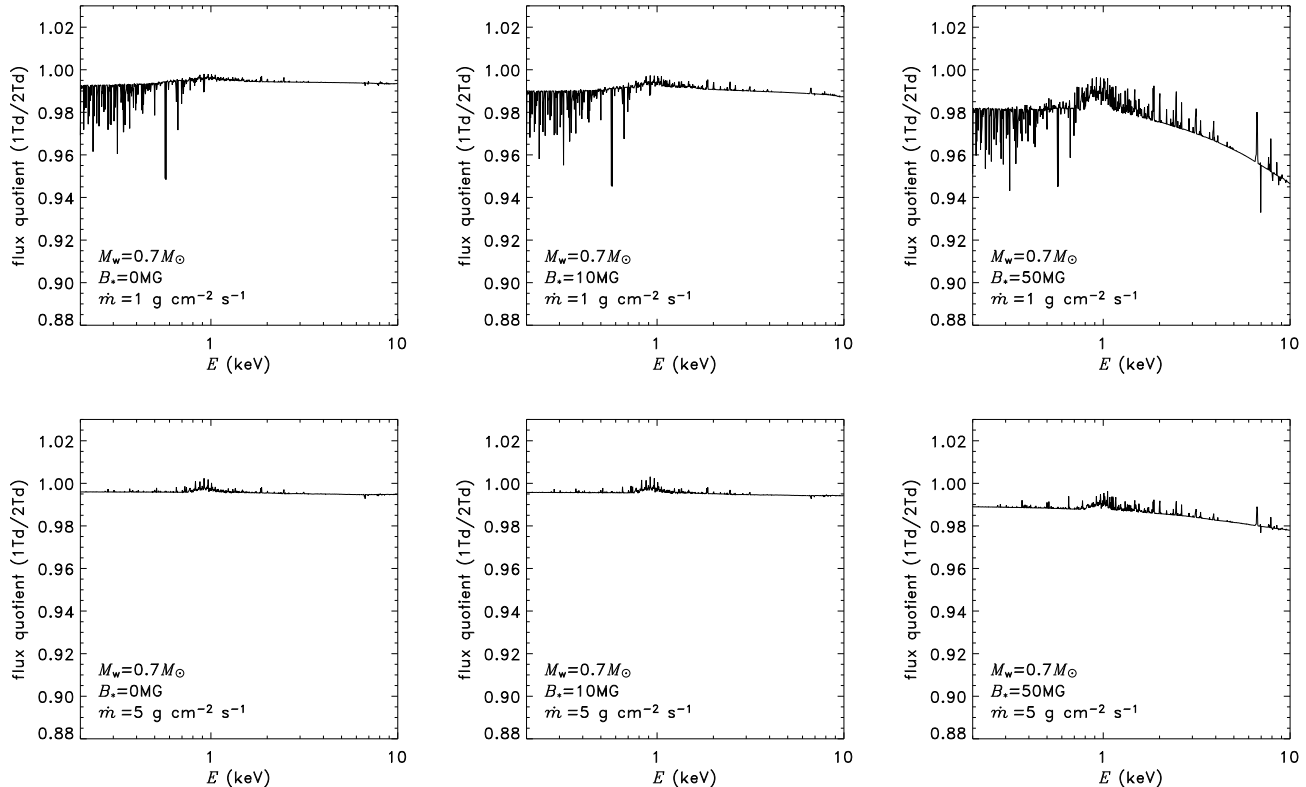


Figure 5. Quotients of spectra in 1T and 2T dipolar models (1Td/2Td). In these cases the white-dwarf mass is $0.7 M_{\odot}$ and accretion occurs onto the pole ($\theta_* = 0^\circ$).

the hot-spot area too. For the present study, it suffices to show that the joint inclusion of 2T phenomena and dipolar geometry can reduce mass estimates by $\lesssim 9\%$ near the Chandrasekhar limit, by $\lesssim 7\%$ near a solar mass, but only $\lesssim 1\%$ near $0.5 M_{\odot}$.

We now consider the mass estimates of Ramsay (2000) who determined the mass of the white dwarf in 21 mCVs – 8 polars and 13 intermediate polars (IPs) – using *RXTE* PCA (2–60 keV) data. Using the 1Tp model prescribed by Cropper et al. (1999), Ramsay (2000) found a mean mass of $0.87M_{\odot}$ and $0.80M_{\odot}$ for his sample of IPs and polars respectively. Applying a correction factor based on our results above gives a mean mass of $0.82M_{\odot}$ and $0.76M_{\odot}$ for the IPs and polars respectively.

Other affects maybe important as well. For instance, Suleimanov et al. (2005) found that when they determined the mass of 14 IPs using *RXTE* PCA plus *HEXTE* (10–200keV) data the mean mass of the IPs was reduced by $0.20M_{\odot}$ to $0.75M_{\odot}$. This was explained by the fact that in IPs broad accretion curtains with high total absorption columns are thought to be present, which can affect the modelling of the continuum even at relatively hard X-ray energies. Because polars have higher magnetic field strengths and hence more collimated accretion streams, absorption may affect their X-ray continua less than for IPs.

We note that the mean mass of white dwarfs in mCVs as determined by Suleimanov et al. (2005) and in this paper is greater than that of isolated white

dwarfs ($0.56M_{\odot}$, Bergeron et al. 1992). We note that Wickramasinghe & Ferrario (2005) found that white dwarfs with high magnetic fields have a mean mass of $0.93M_{\odot}$ – significantly higher than that in isolated white dwarfs. Our mass estimates remain consistent with the scenario in which magnetic white dwarfs are more massive than their non-magnetic counterparts.

4.3 Further applications and scope

Our 2-temperature formulation with magnetic funnel geometry is applicable to a variety of accreting stellar systems other than the cataclysmic variables. With substitution of the relevant radiation processes, the model is applicable to accretion onto neutron stars, and similarly it is applicable to field-aligned accretion onto T Tauri stars. The key assumptions are that the flow be hydrodynamic (collisional), field-aligned, and that radiation effects can be described in terms of local variables.

Our hydrodynamic formulation treats accretion flows that are steady and smooth: rapid temporal variability is omitted. Continuous flows onto some mCVs oscillate at ~ 1 Hz, interpreted as a thermal instability of the shock, (see Langer et al. 1981, 1982; Chevalier & Imamura 1982; Saxton et al. 1998). This is observed optically in only a minority of systems (e.g. Middleditch 1982; Cropper et al. 1986; Imamura & Steiman-Cameron 1986; Larsson 1987, 1989; Ramseyer et al. 1993; Middleditch et al. 1997) but not

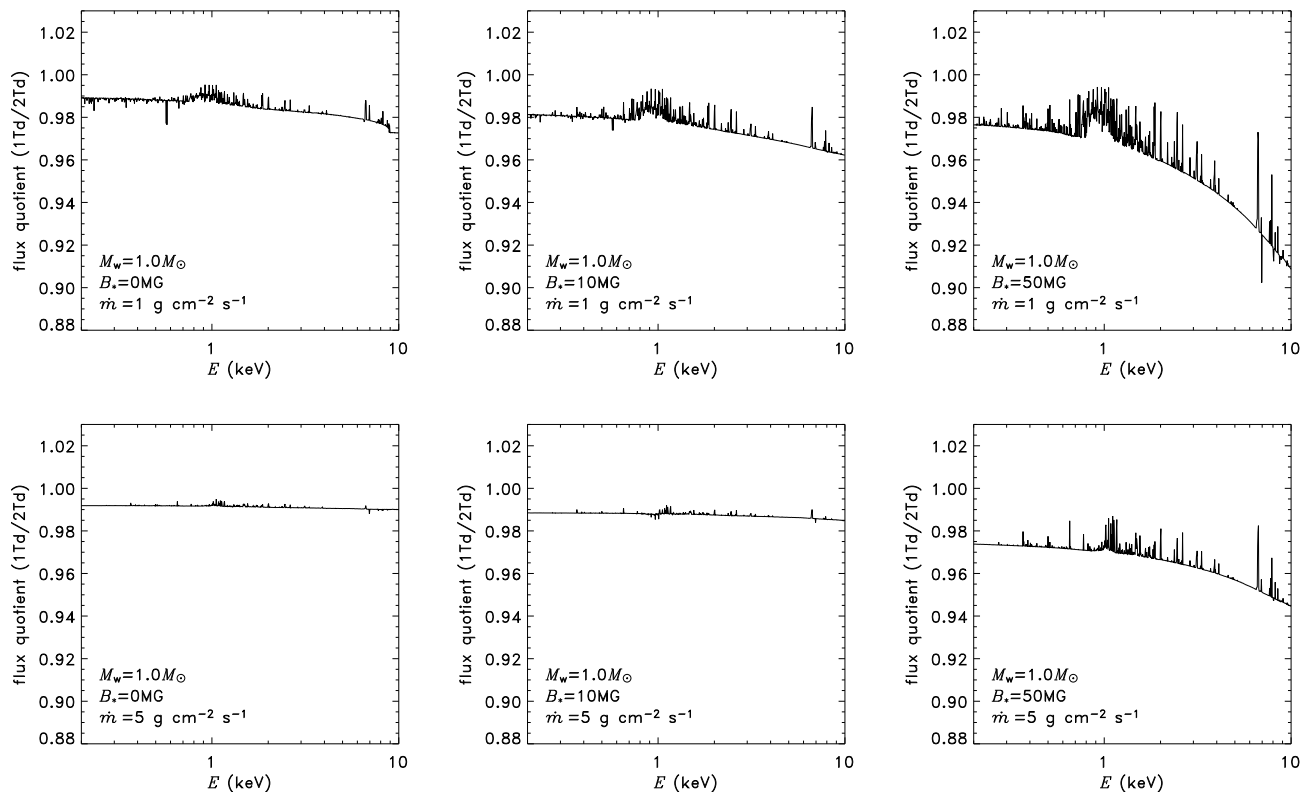


Figure 6. Quotients of spectra in 1T and 2T models (1Td/2Td), as in Figure 5 but with $M_w = 1.0 M_\odot$.

yet in X-rays (e.g. Wolff et al. 1999; Christian 2000). Thus fast oscillations may not affect X-ray spectra at presently observable levels. The absence of a steady structure would preclude collisional ionisation equilibrium, which affects the spectral line strengths, as they critically depend on the density structure (see e.g. Fujimoto & Ishida 1997; Wu et al. 2001). Our model is more applicable to cases with slower temporal variability – flaring which exceeds the post-shock free-fall time – by calculating sequences of steady models with different \dot{m} values but identical M_w , B_* and θ_* .

The spectral effects of spatial variations are harder to assess. Mild inhomogeneities might be modelled by treating the accretion column as a distribution of streams with differing \dot{m} and cross-sections, then summing their spectra. By construction, we cannot model highly inhomogeneous flows: these would require highly resolved, time-dependent hydrodynamic simulations. In some asynchronous accreting systems, a continuous flow may fragment into dense blobs due to a magnetic drag (e.g. Arons & Lea 1980; Frank et al. 1988; King 1993; Wynn & King 1995). However if the magnetic field is strong enough then the blobs shred into a continuous field-aligned flow as they near to the stellar surface (Arons & Lea 1980). If the field is weak, blobs may survive to strike the stellar surface individually. Such a shower is qualitatively different from a pressure-supported stand-off shock. However, emission from steady accretion shocks is universally observed in mCVs and is the major component, except at the softest energies where the emission from ballistic blobs contributes in most cases. Spectral modelling of

predominantly clumpy accretion is a challenge beyond the scope of this paper.

ACKNOWLEDGMENTS

KW thanks TIARA for their hospitality during his visit there and for support through a Visiting Fellowship. TIARA is operated under Academia Sinica and the National Science Council Excellence Projects programs in Taiwan administered through grant number NSC 94-2752-M-007-001.

REFERENCES

- Aizu K., 1973, Prog. Theor. Phys, 49, 1184
- Arfken G. B., Weger H. J., 2001, Mathematical Methods for Physicists. Academic Press, New York
- Arons J., 1993, ApJ, 408, 160
- Arons J., Lea S. M., 1980, ApJ, 235, 1016
- Bergeron P., Saffer R. A., Liebert J., 1992, ApJ, 394, 228
- Canalle J. B. G., Saxton C. J., Wu K., Cropper M., Ramsay G., 2005, A&A, 440, 185
- Chevalier R. A., Imamura J. N., 1982, ApJ, 261, 543
- Christian D. J., 2000, AJ, 119, 1930
- Cropper M., 1990, Space Sci. Rev., 54, 195
- Cropper M., Menzies J. W., Tapia S., 1986, MNRAS, 218, 201
- Cropper M., Wu K., Ramsay G., Kocabiyik A., 1999, MNRAS, 306, 684

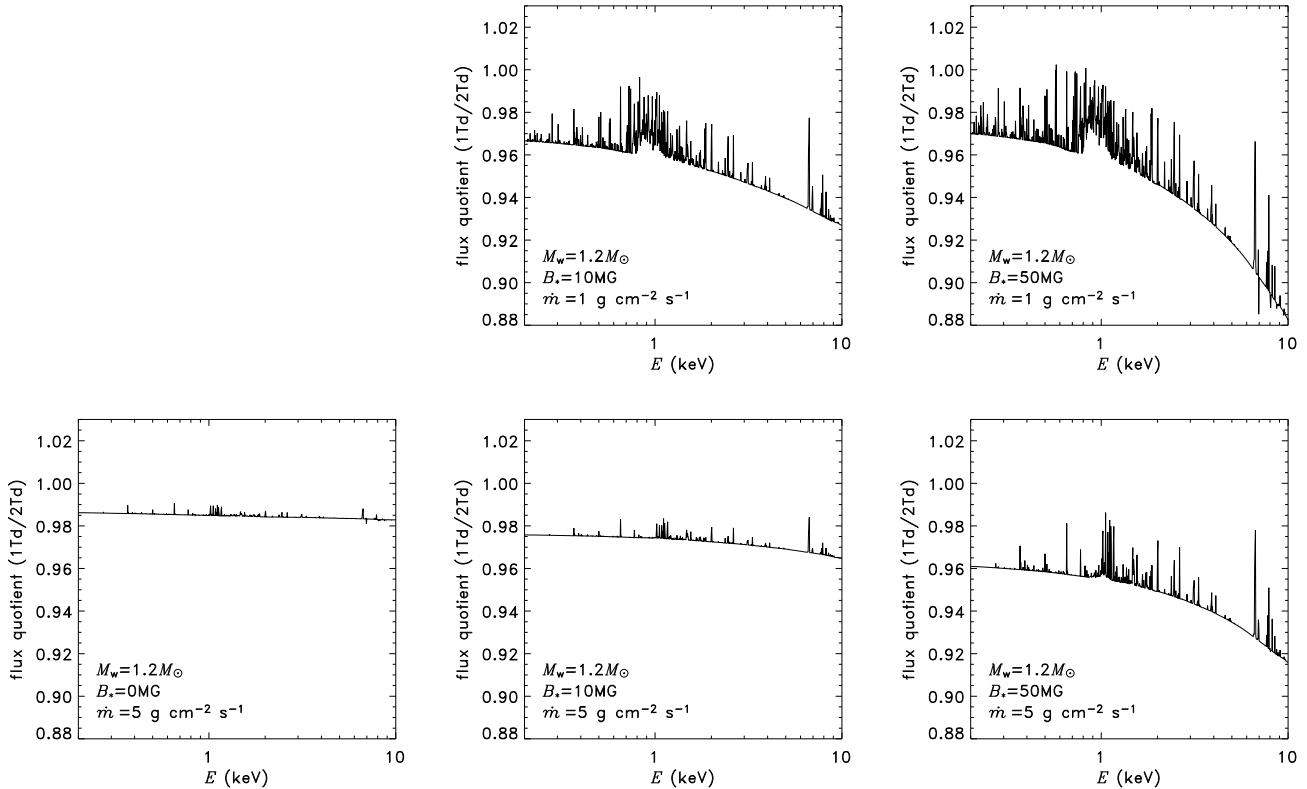


Figure 7. Quotients of spectra in 1T and 2T models (1Td/2Td), as in Figure 5 but with $M_w = 1.2 M_\odot$.

- Elsner R. F., Lamb F. K., 1977, *ApJ*, 215, 897
 Fabian A. C., Pringle J. E., Rees M. J., 1976, *MNRAS*, 175, 43
 Ferrario L., 1996, *PASA*, 13, 87
 Fischer A., Beuermann K., 2001, *A&A*, 373, 211
 Frank J., King A. R., Lasota J.-P., 1988, *A&A*, 193, 113
 Fujimoto R., Ishida M., 1997, *ApJ*, 474, 774
 Ghosh P., Lamb F. K., 1978, *ApJ*, 223, L83
 Gregory S. G., Jardine M., Simpson I., Donati J.-F., 2006, *MNRAS*, 371, 999
 Gullbring E., Calvet N., Muzerolle J., Hartmann L., 2000, *ApJ*, 544, 927
 Hartman L., Hewett R., Calvet N., 1994, *ApJ*, 426, 669
 Heerlein C., Horne K., Schwope A. D., 1999, *MNRAS*, 304, 145
 Imamura J. N., 1981, PhD thesis, Indiana University, U.S.A.
 Imamura J. N., Aboasha A., Wolff M. T., Kent K. S., 1996, *ApJ*, 458, 327
 Imamura J. N., Durisen R. H., Lamb D. Q., Weast G. J., 1987, *ApJ*, 313, 298
 Imamura J. N., Steiman-Cameron T. Y., 1986, *ApJ*, 311, 786
 Kaastra J. S., Mewe R., 1993, *A&AS*, 97, 443
 King A. R., 1993, *MNRAS*, 261, 144
 King A. R., Lasota J. P., 1979, *MNRAS*, 188, 653
 Koldoba A. V., Lovelace R. V. E., Ustyugova G. V., Romanova M. M., 2002, *AJ*, 123, 2019
 Königl A., 1991, *ApJ*, 370, L39
 Kryukov I. A., Pogorelov N. V., Bisnovatyi-Kogan G. S., Anzer U., Börner G., 2000, *A&A*, 364, 901
 Lamb D. Q., Masters A. R., 1979, *ApJ*, 234, L117
 Lamzin S. A., Stempels H. C., Piskunov N. E., 2001, *A&A*, 369, 965
 Langer S. H., Chanmugam G., Shaviv G., 1981, *ApJ*, 245, L23
 Langer S. H., Chanmugam G., Shaviv G., 1982, *ApJ*, 258, 289
 Larsson S., 1987, *A&A*, 181, L15
 Larsson S., 1989, *A&A*, 217, 146
 Li J., Wickramasinghe D. T., Rüdiger G., 1996, *ApJ*, 469, 765
 Li J., Wilson G., 1999, *ApJ*, 527, 910
 Lovelace R. V. E., Romanova M. M., Bisnovati-Kogan G. S., 1995, *MNRAS*, 275, 244
 Mewe R., Gronenschild E. H. B. M., van den Oord G. H. J., 1985, *A&AS*, 62, 197
 Middleditch J., 1982, *ApJ*, 257, L71
 Middleditch J., Imamura J. N., Steiman-Cameron T. Y., 1997, *ApJ*, 489, 912
 Nauenberg M., 1972, *ApJ*, 175, 417
 Ramsay G., 2000, *MNRAS*, 314, 403
 Ramsay G., Cropper M., Hellier C., Wu K., 1998, *MNRAS*, 297, 1269
 Ramseyer T. F., Robinson E. L., Zhang E., Wood J. H., Stiening R. F., 1993, *MNRAS*, 260, 209
 Romanova M. M., Ustyugova G. V., Koldoba A. V., Wick J. V., Lovelace R. V. E., 2003, *ApJ*, 595, 1009

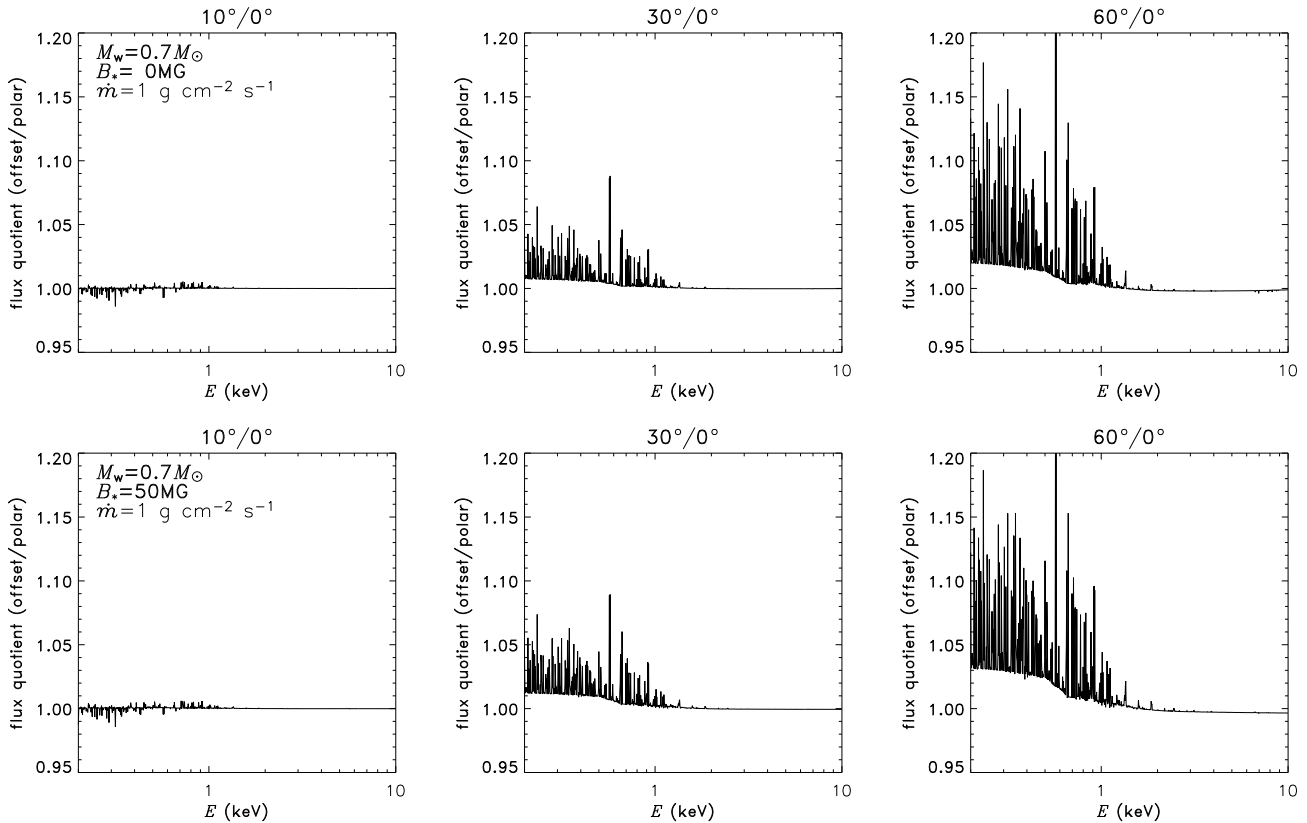


Figure 8. The effect of accretion latitude. Quotients of spectra show different colatitudes of the accretion hot-spot: $10^\circ/0^\circ$, $30^\circ/0^\circ$ and $60^\circ/0^\circ$ for left, middle and right columns respectively. The upper panels show cases with weaker magnetic fields; the lower panels show cases with stronger fields. In these cases the white-dwarf mass is $0.7 M_\odot$ and the specific accretion rate is $\dot{m} = 1 \text{ g cm}^{-2} \text{ s}^{-1}$. All else being equal, accretion further from the pole enhances the soft X-ray continuum and lines.

Rybicki G. B., Lightman A. P., 1979, *Radiative Processes in Astrophysics*. Wiley, New York
 Saxton C. J., Wu K., 1999, *MNRAS*, 310, 677
 Saxton C. J., Wu K., 2001, *MNRAS*, 324, 659
 Saxton C. J., Wu K., Cropper M., Ramsay G., 2005, *MNRAS*, 360, 1091
 Saxton C. J., Wu K., Pongracic H., 1997, *PASA*, 14, 164
 Saxton C. J., Wu K., Pongracic H., Shaviv G., 1998, *MNRAS*, 299, 862
 Spitzer L., 1962, *Physics of Fully Ionized Gases*, 2nd Ed.. Interscience, New York
 Stelzer B., Schmitt J. H. M. M., 2004, *A&A*, 418, 687
 Suleimanov V., Revnivtsev M., Ritter H., 2005, *A&A*, 435, 191
 Toropina O. D., Romanova M. M., Toropin Y. M., Lovelace R. V. E., 2003, *ApJ*, 593, 472
 Warner B., 1995, *Cataclysmic Variable Stars*. Cambridge University Press, Cambridge
 Wickramasinghe D. T., Ferrario L., 2005, *MNRAS*, 356, 1576
 Woelk U., Beuermann K., 1996, *A&A*, 306, 232
 Wolff M. T., Imamura J. N., Middleditch J., Wood K. S., Steiman-Cameron T., 1999, in Hellier C., Mukai K., eds, *ASP Conf. Ser.* 157 p. 149
 Wu K., 1994, *PASA*, 11, 61
 Wu K., 2000, *Space Sci. Rev.*, 93, 611

Wu K., Chanmugam G., Shaviv G., 1994, *ApJ*, 426, 664
 Wu K., Cropper M., Ramsay G., 2001, *MNRAS*, 327, 208
 Wu K., Cropper M., Ramsay G., Saxton C., Bridge C., 2003, *ChJAA*, 3 Suppl., 235
 Wynn G. A., King A. R., 1995, *MNRAS*, 275, 9

APPENDIX A: COORDINATE SYSTEM

Following Canalle et al. (2005), we adopt a curvilinear coordinate system (u, w, φ) in which φ is an azimuthal angle about the polar axis, w is a path-length along a magnetic field line, and u measures along an equipotential transverse to the field lines, effectively choosing the latitude of the field-line's footprint on the stellar surface. The dipolar coordinates correspond to conventional polar coordinates according to

$$u = \frac{\sin^2 \theta}{r} \quad \text{and} \quad (\text{A1})$$

$$w = \frac{\cos \theta}{r^2}, \quad (\text{A2})$$

implying that

$$w^2 r^4 + ur - 1 = 0. \quad (\text{A3})$$

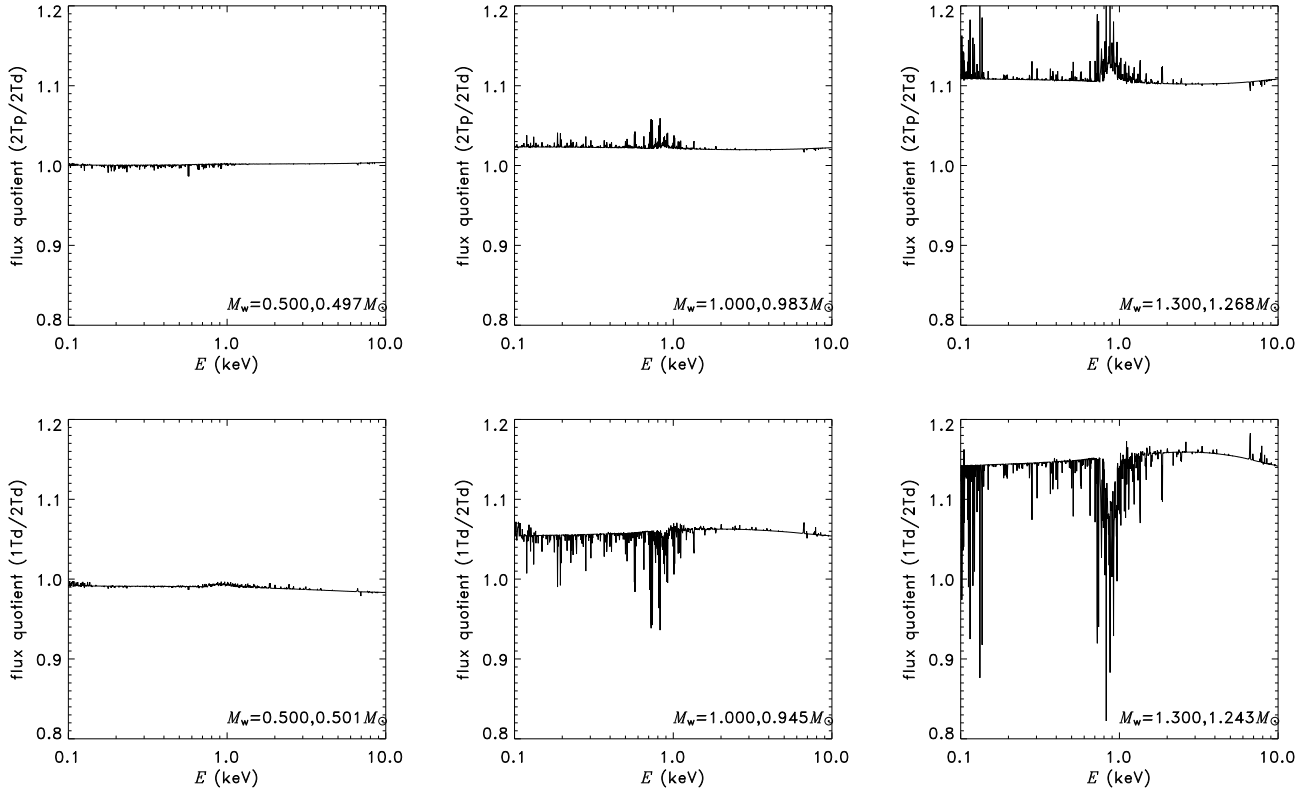


Figure 9. Matching the X-ray continua of two different accretion models requires different M_w values. The top row compares 2T planar and dipolar models. The bottom row compares 1T dipolar and 2T dipolar models. Masses were adjusted to achieve approximately proportional continua (flat quotient profile). We have fixed $B_* = 50\text{MG}$, $\dot{m} = 2 \text{ g cm}^{-2} \text{ s}^{-1}$ and $\theta_* = 0^\circ$. For low M_w (left panels) the inferred masses are similar; but for more massive cases the model masses differ appreciably.

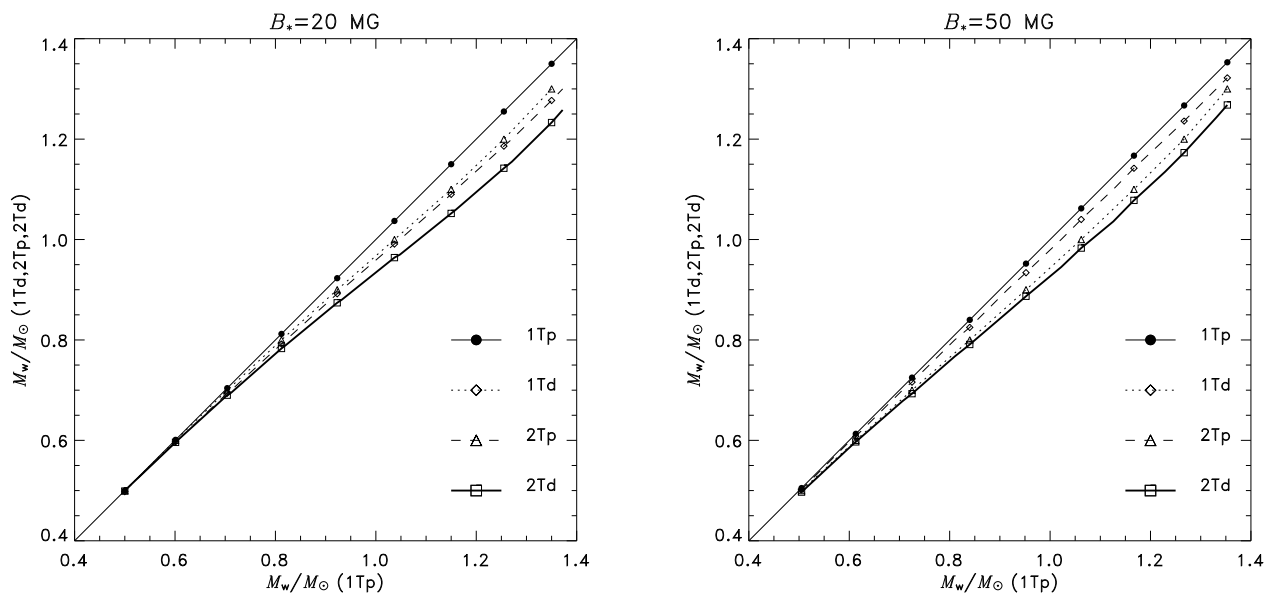


Figure 10. Masses inferred by fitting continua of 1Tp, 1Td, 2Tp and 2Td models to each other. Radially variable gravity, a dipolar accretion funnel and two-temperature effects yield harder spectra for lower M_w values. Here we have fixed the hot-spot size and $\dot{m} = 2 \text{ g cm}^{-2} \text{ s}^{-1}$. Symbols indicate $0.1M_\odot$ steps in the 2Tp model; the curves are thin/ \bullet (1Tp), dotted/ Δ (2Tp), dashed/ \diamond (1Td) and thick/ \square (2Td).

Table 2. Sets of M_w values that give comparable spectral continua, calculated for the 1Tp, 1Td, 2Tp and 2Td models. The latter imply similar or lower masses. For these mass fits, we fix $\dot{m} = 2 \text{ g cm}^{-2} \text{ s}^{-1}$ and $\theta_* = 0^\circ$.

$B_* = 20 \text{ MG}$			
1Tp	1Td	2Tp	2Td
0.500	0.498	0.500	0.499
0.601	0.597	0.600	0.596
0.704	0.694	0.700	0.690
0.812	0.792	0.800	0.783
0.923	0.892	0.900	0.874
1.037	0.991	1.000	0.964
1.150	1.090	1.100	1.052
1.255	1.186	1.200	1.142
1.350	1.277	1.300	1.233

$B_* = 50 \text{ MG}$			
1Tp	1Td	2Tp	2Td
0.505	0.502	0.500	0.497
0.613	0.608	0.600	0.597
0.725	0.716	0.700	0.693
0.840	0.825	0.800	0.791
0.952	0.934	0.900	0.887
1.062	1.040	1.000	0.983
1.167	1.142	1.100	1.078
1.267	1.236	1.200	1.173
1.353	1.322	1.300	1.268

We scale the coordinate axes so that the stellar surface occurs at $r = 1$. The transformation to Cartesian coordinates obeys

$$\begin{bmatrix} x \\ y \\ z \end{bmatrix} = \begin{bmatrix} \sqrt{wr^3} \cos \varphi \\ \sqrt{wr^3} \sin \varphi \\ wr^3 \end{bmatrix}. \quad (\text{A4})$$

The orthogonal unit vectors, $(\hat{u}, \hat{w}, \hat{\varphi})$, vary spatially. Locally they transform into their Cartesian counterparts $(\hat{i}, \hat{j}, \hat{k})$ according to

$$\begin{bmatrix} \hat{u} \\ \hat{w} \\ \hat{\varphi} \end{bmatrix} = \mathbf{U} \begin{bmatrix} \hat{i} \\ \hat{j} \\ \hat{k} \end{bmatrix}. \quad (\text{A5})$$

where (see e.g. Arfken & Weger 2001) the transformation matrix is

$$\mathbf{U} \equiv \begin{bmatrix} \frac{1}{h_1} \frac{\partial x}{\partial u} & \frac{1}{h_1} \frac{\partial y}{\partial u} & \frac{1}{h_1} \frac{\partial z}{\partial u} \\ \frac{1}{h_2} \frac{\partial x}{\partial w} & \frac{1}{h_2} \frac{\partial y}{\partial w} & \frac{1}{h_2} \frac{\partial z}{\partial w} \\ \frac{1}{h_3} \frac{\partial x}{\partial \varphi} & \frac{1}{h_3} \frac{\partial y}{\partial \varphi} & \frac{1}{h_3} \frac{\partial z}{\partial \varphi} \end{bmatrix}. \quad (\text{A6})$$

The coefficients h_1 , h_2 and h_3 comprising the metric of the curvilinear coordinates system, are defined by

$$h_{[1,2,3]}^2 \equiv \left(\frac{\partial x}{\partial [u, w, \varphi]} \right)^2 + \left(\frac{\partial y}{\partial [u, w, \varphi]} \right)^2 + \left(\frac{\partial z}{\partial [u, w, \varphi]} \right)^2, \quad (\text{A7})$$

with explicit functional forms given in Canalle et al. (2005). For a small fluid element following a magnetic field line, its transverse area varies as $h_1 h_3$ in response to the converge

of the field. The rate of convergence of the field lines, and thus the lateral compression of field-channelled inflow, can be expressed in terms of a function

$$\mathcal{H} \equiv \frac{\partial}{\partial w} \ln(h_1 h_3). \quad (\text{A8})$$

APPENDIX B: NUMERICAL SOLUTION

We find that it is convenient to express the post-shock structure in terms of a specific entropy variable,

$$s \equiv P \rho^{-\gamma} = \left(\frac{h_1 h_3}{C} \right)^{\gamma-1} (\xi - v) v^\gamma, \quad (\text{B1})$$

which has a gradient equation,

$$\frac{ds}{dw} = - \frac{(\gamma - 1) \tilde{\Lambda} s}{(\xi - v) v^{5/2}} = -(\gamma - 1) \left(\frac{h_1 h_3}{C} \right)^{\gamma-1} \tilde{\Lambda} v^{\gamma-5/2}. \quad (\text{B2})$$

Since the expression (B2) never changes sign, the spatial variation of s is guaranteed to be monotonic throughout the post-shock flow. The maximum value of s occurs at the shock; the specific entropy falls to zero at the stellar surface. Thus s is a convenient replacement for w in the role of independent, integration variable. Differential equations in terms of ds are obtained by multiplying dw/ds into (18), (19), (20) and (21) and then simplifying algebraic terms to reduce numerical round-off errors.

The strong shock boundary conditions imply that

$$v_s = \frac{1}{4\sqrt{R_s}} \quad (\text{B3})$$

and

$$\xi_s = \frac{1}{\sqrt{R_s}}, \quad (\text{B4})$$

(Canalle et al. 2005), where we use a unit convention based on $C = 1$, the stellar radius $R_w = 1$ and superficial escape velocity $V_w \equiv \sqrt{2GM_w/R_w} = 1$. The shock values of s and P_e follow from (B1) and (14), with σ_s treated as a free parameter. Assuming trial estimates of the shock location, we integrate inwards to $s \rightarrow 0$ and check for consistency between this inner radius and the stellar surface, $r = 1$. A numerical root-finder iterates to a value of R_s that matches both boundary conditions.

This paper has been typeset from a $\text{T}_{\text{E}}\text{X}/\text{L}^{\text{A}}\text{T}_{\text{E}}\text{X}$ file prepared by the author.